



HAL
open science

Validating heat balance models for tungsten dust in cold dense plasmas

Ladislav Vignitchouk, Svetlana Ratynskaia, Mikhail Kantor, P. Talias, Marco de Angeli, H van Der Meiden, Vernimmen J, F. Brochard, Andrey Shalpegin, Thoren E., et al.

► To cite this version:

Ladislav Vignitchouk, Svetlana Ratynskaia, Mikhail Kantor, P. Talias, Marco de Angeli, et al.. Validating heat balance models for tungsten dust in cold dense plasmas. *Plasma Physics and Controlled Fusion*, 2018, 60 (11), 10.1088/1361-6587/aadbcb . hal-02372199

HAL Id: hal-02372199

<https://hal.univ-lorraine.fr/hal-02372199>

Submitted on 20 Nov 2019

HAL is a multi-disciplinary open access archive for the deposit and dissemination of scientific research documents, whether they are published or not. The documents may come from teaching and research institutions in France or abroad, or from public or private research centers.

L'archive ouverte pluridisciplinaire **HAL**, est destinée au dépôt et à la diffusion de documents scientifiques de niveau recherche, publiés ou non, émanant des établissements d'enseignement et de recherche français ou étrangers, des laboratoires publics ou privés.



Distributed under a Creative Commons Attribution - NonCommercial - NoDerivatives 4.0 International License

Validating heat balance models for tungsten dust in cold dense plasmas

L. Vignitchouk^a, S. Ratynskaia^a, M. Kantor^b, P. Tolias^a, M. De Angeli^c, H. van der Meiden^d, J. Vernimmen^d, F. Brochard^e, A. Shalpegin^e, E. Thorén^a, J.-P. Banon^f

^a Space and Plasma Physics, KTH Royal Institute of Technology, Stockholm, Sweden

^b Ioffe Institute, St. Petersburg 194021, Russia

^c Istituto di Fisica del Plasma “Piero Caldirola” — CNR, Via Cozzi 53, 20125 Milano, Italy

^d FOM Institute DIFFER, Dutch Institute For Fundamental Energy Research, De Zaale 20, 5612AJ Eindhoven, The Netherlands

^e Université de Lorraine, Institut Jean Lamour, UMR 7198 CNRS, F-54506, Vandoeuvre-lès-Nancy, France

^f Department of Physics, NTNU Norwegian University of Science and Technology, NO-7491 Trondheim, Norway

E-mail: ladislas.vignitchouk@ee.kth.se

Abstract. The first comparison of dust radius and surface temperature estimates, obtained from spectroscopic measurements of thermal radiation, with simulations of dust heating and vaporization by the MIGRAINE dust dynamics code is reported. The measurements were performed during controlled tungsten dust injection experiments in the cold and dense plasmas of Pilot-PSI, reproducing ITER divertor conditions. The comparison has allowed us to single out the dominating role of the work function contribution to the dust heating budget. However, in the plasmas of interest, dust was found to enter the strong vaporization regime, in which its temperature is practically insensitive to plasma properties and the various uncertainties in modelling. This makes the dust temperature a poor figure of merit for model validation purposes. On the other hand, simple numerical scalings obtained from orbital-motion-limited estimates were found to be remarkably robust and sufficient to understand the main physics at play in such cold and dense plasmas.

This is an author-created, un-copyedited version of an article accepted for publication/published in Plasma Physics and Controlled Fusion. IOP Publishing Ltd is not responsible for any errors or omissions in this version of the manuscript or any version derived from it. The Version of Record is available online at [10.1088/1361-6587/aadbcb](https://doi.org/10.1088/1361-6587/aadbcb)

1. Introduction

Dust dynamics codes have been employed for more than a decade to study dust transport and vaporization in contemporary fusion devices as well as ITER. Building on the foundations laid out by the pioneering code DUSTT [1, 2], most of the codes currently available [3–6] are based on the orbital motion limited (OML) framework [7] or some extension thereof, with the exception of the MIGRAINE code, whose model has been recently updated to treat dust charging and heating in the presence of a strong magnetic field [8, 9]. The OML approach is attractive because it yields a simple yet complete kinetic description of the perturbed plasma region surrounding a spherical dust grain, from which all quantities of interest, such as particle currents and heat fluxes, can be derived. Nevertheless, OML calculations rely on numerous assumptions on the background plasma, which are often violated in dense magnetized fusion plasmas.

The output of nearly all dust dynamics codes has been subject to comparisons against experimental data, often resulting in claims of successful model validation. However, the usefulness of such comparisons for metallic dust, which is the focus of current research in light of the all-metal ITER wall design, is questionable. Although the first detailed measurements of intrinsic carbon dust motion in NSTX [10] and DIII-D [11] have provided valuable insight on dust dynamics and particularly on the importance of the ion drag force, the ability to reproduce observable dust trajectories via simulations often brings little information on the validity of the underlying models. This is especially true for heavy metallic dust, whose motion across the typical observation windows is largely inertial and subject to significant uncertainties in regard to initial conditions such as dust size and velocity, even in controlled dust injection experiments [5, 12]. The inertial motion property actually has some advantages for predictive studies of tungsten (W) dust or large beryllium (Be) droplets since it provides certainty on the trajectories, and hence on the plasma background successively sampled by the particles as they move across electron density and temperature gradients. On the other hand, it greatly undermines the utility of trajectory tracking [10, 11, 13] — the main and often only dust diagnostics available — to the validation of dust heating and ablation models, essentially leaving the measured lifetime of glowing particles as the only ex-

ploitable data.

In fact, the observed dust lifetimes in fusion environments are consistently underestimated by OML-based simulations [5, 12, 14, 15], a trend which is sometimes compensated by ad hoc numerical remedies such as allowing for arbitrary large dust sizes [14] or the inclusion of a heat reduction coefficient [15]. On the theoretical front, several physical mechanisms have been proposed to explain these discrepancies, such as thin-sheath ion collection [16, 17], space-charge limitations of electron emission [17, 18], the influence of the background magnetic field on incoming [8] and emitted [19] electrons, and vapour shielding [20, 21].

For studies of dust in ITER, the micro-physics of electron and ion absorption have to be brought into discussion along with the numerous processes mentioned above. Indeed, quantum-mechanical particle-solid interactions can only be neglected when the plasma temperature exceeds by far the characteristic binding energies of the system. When this condition is not satisfied, heating due to micro-physical processes occurring in the Ångström vicinity of the dust surface dominates the contribution of the absorbed particles' kinetic energy. This is the case for the main environments of interest to dust and droplet dynamics in ITER: detached divertor plasmas in which the temperature is of the order of a few eV, and mitigated disruption scenarios in which the stored ionization energy of multiply charged mitigating species typically lies in the 100–1000 eV range [9].

The purpose of this work is to gain insight into the heat balance of W dust in high-density, low-temperature plasmas similar to those expected in the ITER divertor. We report on the first systematic comparison between experimental estimations of dust size and surface temperature derived from spectroscopic measurements of thermal radiation [22] and theoretical predictions. The measurements have been carried out during controlled W dust injection experiments in Pilot-PSI [23, 24] and complemented by simultaneous camera observations. After a presentation of the main experimental results, we conduct a critical examination of the temperature and size measurement accuracy, as well as the extent to which the theoretical OML scalings can be employed to single out the dominant contributions to dust heating and survivability.

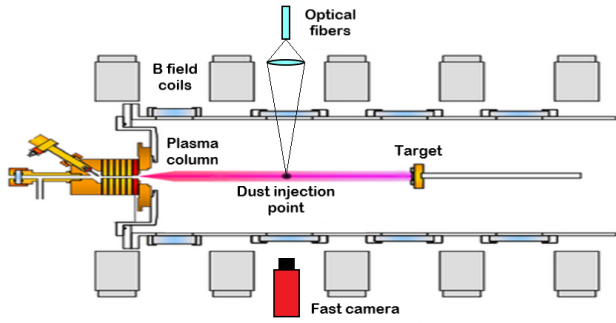


Figure 1. Top view of Pilot-PSI showing the position of the Photron fast camera and the optical fiber bundle.

2. Experimental layout and methodology

2.1. Dust injection and spectroscopic measurements

Spherical W dust was injected by an electrically driven piezo-electric dispenser located approximately 2 m above the center of the Pilot-PSI plasma beam [23,24]. For the majority of the plasma shots, the injected dust was meshed to ensure a monodisperse population with diameter $9 \pm 1 \mu\text{m}$; in some cases, the original size distribution was used, ranging from $5 \mu\text{m}$ to $25 \mu\text{m}$ in diameter. After their entry in the plasma, the glowing particles were observed by a Photron FASTCAM fast camera with horizontal line of sight through the center of the plasma column, as shown in figure 1. After subtraction of the visible plasma background, camera images such as those shown in figure 2 were post-processed using the TRACE code [25], which allows to track the individual particles and reconstruct their trajectories projected onto the vertical mid-plane.

The light emitted from a region of width $\sim 1.2 \text{ mm}$ and height $\sim 50 \text{ mm}$ directly below the injection point (see figure 2) was also collected by a f/1.8 Nikon objective of 55 mm aperture within a viewing angle of 0.21 rad, then fed to a Jobin & Ivon spectrometer THR 1000 with grating 150 l mm^{-1} via an optical fiber bundle (38 fibers of diameter $400 \mu\text{m}$ with $50 \mu\text{m}$ gaps), resulting in a spectral resolution of 6.88 nm mm^{-1} . The spectrometer output was then transmitted to a Phantom V12 fast camera so as to produce spectrally resolved images as in figure 3. During each shot, dust emission was measured at a sampling rate between 1 kHz and 5 kHz, over one of the four available spectral ranges: 360–530 nm, 420–590 nm, 480–650 nm and 530–700 nm.

2.2. Plasma parameters

The discharge current and hydrogen flow rate from the Pilot-PSI nozzle were varied between shots so as to produce plasmas with different densities and temperatures. The magnetic field was maintained at

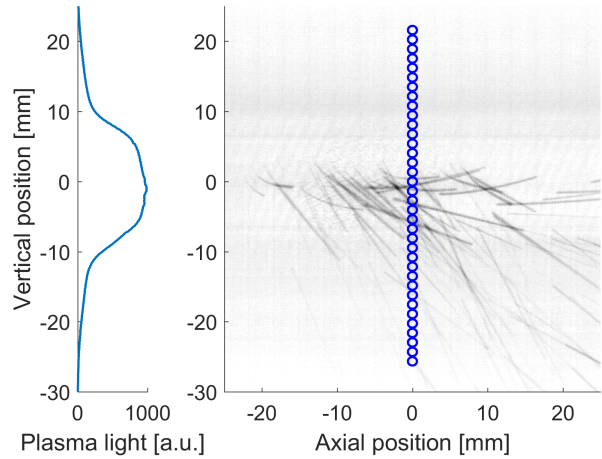


Figure 2. Superposition of successive negative camera images of dust trajectories after subtraction of the background plasma light shown on the left. The viewing area of the individual optical fibers is represented by blue circles.

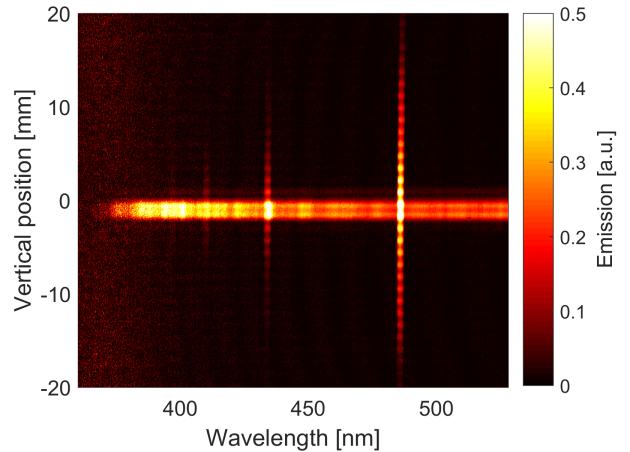


Figure 3. Typical output of the spectroscopic measurement system, shown here for shot #196. Plasma light appears as vertical lines (localized in wavelength but spread in space), whereas thermal radiation from the heated dust manifests as wide horizontal bands (spread in wavelength but localized in space).

0.8 T and Thomson scattering (TS) measurements of the electron density and temperature profiles near the source were carried out at every modification of the discharge parameters. The main information is summarized in table 1 and the three representative electron density and temperature profiles are presented in figure 4.

2.3. Dust temperature and radius estimations

After exclusion of the plasma Balmer lines, measured thermal radiation spectra S were fitted against a gray-body law

Shot #	Current [A]	Flow rate [SLM]	TS	Dust diameter [μm]	Spectrometer range [nm]	Spectral measurements	Excluded measurements
189	170	2.5	✓	8–10	480–650	1110	39
190	”	”		”	”	337	25
191	”	”		”	”	323	45
194	190	1.5		”	360–530	N/A ^a	N/A
196	”	”	✓	”	”	N/A ^a	N/A
197	”	”		”	480–650	149	20
209	200	8	✓	5–25	530–700	N/A ^b	N/A

^a Anomalous emission signals over the entire spectrometer range.

^b Large spread in the injected dust size population.

Table 1. Pilot-PSI shots analyzed in this paper. The discharge current and hydrogen volumetric flow rate are given, and shots complemented by TS measurements of the electron density and temperature profiles are indicated. The last columns detail the injected dust size population and the spectroscopic measurement statistics. Observed particles are excluded from the data sets when their fitted temperature is above 7000 K, or their fitted radius is above 10 μm .

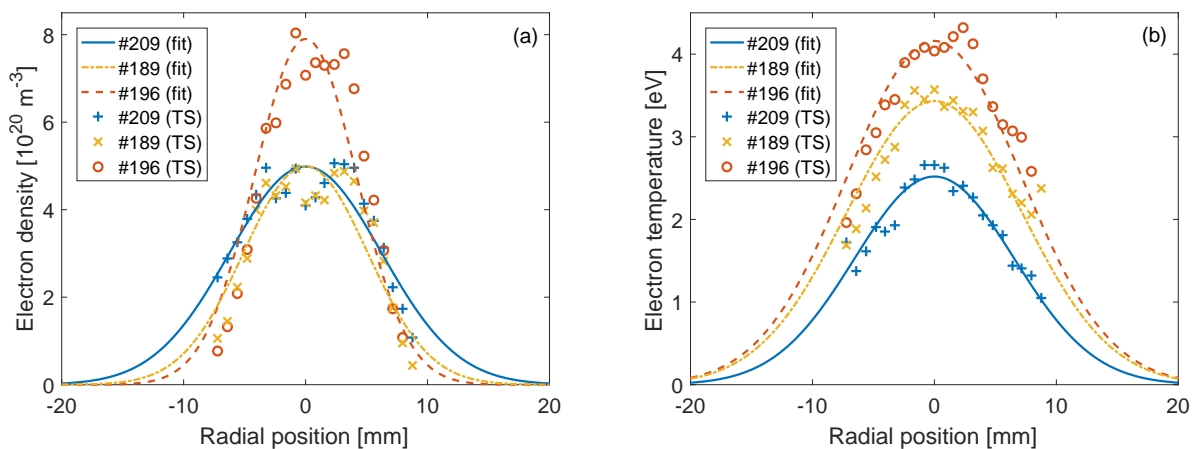


Figure 4. TS measurements of the three representative plasma shots, along with the corresponding gaussian fits used in MIGRAINE simulations. The experimental uncertainty on the TS signals is approximately of the same size as the plotting symbols.

$$S(R_d, T_d, \lambda) = \pi R_d^2 \Delta\Omega \varepsilon(R_d, T_d, \lambda) P(T_d, \lambda) \quad (1)$$

where λ is the wavelength, R_d the dust radius, T_d the dust temperature, P the Planck radiance, ε the spectral emissivity, and $\Delta\Omega$ is the known solid angle subtended by the viewing apparatus. The spectral emissivity of spherical W particles was tabulated from Mie theory calculations [26] and analytic fits of the temperature- and wavelength-dependent optical properties of bulk W [27].

In all the following, we treat the values of R_d and T_d resulting from a nonlinear weighted least-squares fit against (1) as measurements of the dust radius and temperature. The measured experimental

uncertainties of the spectrometric data were translated into error bars on the fitted values by using the inverse Hessian of the sum of squared residuals as an estimate for the covariance matrix. However, it should be noted that the wavelength ranges used in the measurements were generally too narrow to capture the main shape of the thermal spectra. In particular, the measured spectra were mostly monotonic in λ and the Wien-like maximum was either badly resolved or outside the observed range. For this reason, the effects of varying dust size and temperature become difficult to distinguish on the theoretical curves, leading to a strong artificial correlation between the fitted R_d and T_d . Nevertheless, the estimated uncertainties are smaller than the

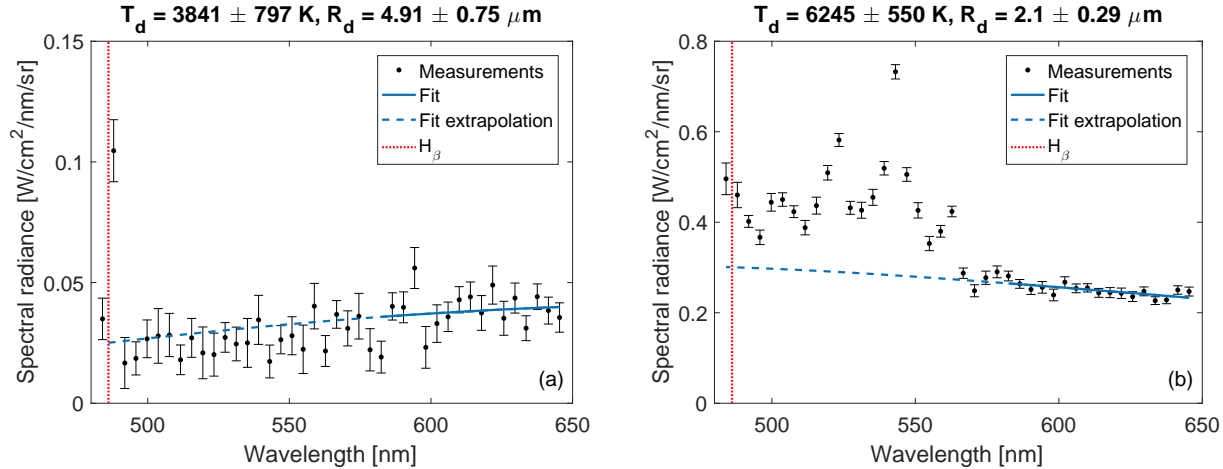


Figure 5. Examples of measured dust spectra from shot #197. (a) Spectrum associated with cold dust; the plasma H_β line is well resolved. (b) Spectrum associated with hot dust; anomalous emission is observed over a large spectral region and is interpreted as line radiation from vaporized W. The fits against (1) were carried out only for $\lambda \geq 580$ nm (solid lines) to exclude anomalous emission. The resulting values of R_d and T_d are shown above each figure.

statistical spread due to the multiplicity of observed dust trajectories (see section 3.2). Moreover, the fitted values of T_d were found to be much more robust to spectroscopic measurement uncertainties than those of R_d ; the median uncertainties estimated by the fitting procedure being 5% and 15%, respectively.

During shots #194–197 — i.e. those with the highest density and temperature — anomalous radiation was measured in the spectral band $\lambda \leq 580$ nm. These signals were interpreted as evidence of ionized W atoms stemming from dust vaporization and were excluded from the data of shot #197 by restricting the fitting procedure to $\lambda > 580$ nm, as detailed in figure 5. In the case of shots #194–196, such restriction was impossible due to the limited spectrometer range, hence the results for these shots are not presented in this paper.

3. Simulation scheme

3.1. Dust-plasma interaction model

Given the plasma profiles shown in figure 4, the representative electron Debye lengths and Larmor radii in the experiment are $\lambda_{De} = 0.5\text{--}2 \mu\text{m}$ and $R_{Le} = 2.5\text{--}6 \mu\text{m}$, respectively. This implies that dust-plasma interaction belongs to the intermediate parameter regime $\lambda_{De} \lesssim R_d \lesssim R_{Le}$ where, strictly speaking, neither the OML description (which assumes $R_d \ll \lambda_{De}, R_{Le}$) nor the updated MIGRAINE model [8] for strong magnetic fields (which assumes $R_d \gg \lambda_{De}, R_{Le}$) is adequate.

The violation of the thick-sheath condition $R_d \ll \lambda_{De}$ implies that the collection of the attracted

plasma species (e.g. ions for negatively charged dust) is impeded by so-called absorption radius effects [17] while the collection of the repelled species is unaffected [28]. As will be discussed later, the presence of thermionic emission currents implies that, in the central region of the plasma column, the floating potential of hot W dust lies near the plasma potential, in which case the ion contribution is negligible. The influence of the magnetic field on electron collection is more difficult to assess, but since background electrons are never strongly magnetized and the magnetic field effect weakens as the dust particles shrink due to vaporization, the model of [8] would be overly conservative and OML predictions are expected to hold with respect to the accuracy of the experimental data. However, it is important to note that this reasoning is invalid for thermionic electrons, whose characteristic energy is of the order of T_d . This point is discussed in details in section 5.3.

In light of the above, simulations reported in this work have been carried out with the OML version of MIGRAINE as presented in [6], with the inclusion of updated low-energy quasi-elastic electron reflection from W, using the reflection yields reported in [29, 30]. The formulas used to describe all physical processes accounted for in MIGRAINE are given in full detail in [6, 30] and the OML expressions that are the most relevant to our analysis are provided in appendix. Here, we only recapitulate the list of charging, heating and momentum transfer mechanisms included in the present simulations. Dust motion is driven by gravity and the ion drag force stemming from the bulk flow velocity of the plasma column along the axial and azimuthal directions. Dust charging is

due to electron collection, ion collection, thermionic emission, secondary electron emission and low-energy quasi-elastic electron reflection. Dust heating includes the kinetic energy and binding energy contributions of the five aforementioned charging processes, as well as the backscattering of neutralized ions, the emission of thermal radiation, and vaporization cooling.

The importance of the micro-physical processes occurring in the vicinity of the dust surface — particularly the release of binding energies upon plasma species collection — and their contribution to dust heating deserves particular attention in our study. These processes are typically ignored or only partially included in dust dynamics codes, on the basis of their small influence on dust heating in scrape-off layer environments. However, they can be substantial or even dominant in divertor conditions. When an incoming electron with kinetic energy E_{inc} is collected, the polarization of the valence electrons creates an image force which continuously accelerates the collected electron to the inner metal potential [29]. The electron then equilibrates with the lattice at the bulk temperature T_{d} , resulting in a net increase of the dust thermal energy by approximately $E_{\text{inc}} + W_{\text{f}} - T_{\text{d}} \simeq E_{\text{inc}} + W_{\text{f}}$. A similar reasoning can be applied to collected ions, with the difference that the work function has to be replaced by the surface binding energy U_{sb} . In addition, collected ions recombine with bound electrons upon reaching the surface of the dust particle. In the case of singly charged ions, this further heats up the dust by $U_{\text{iz}} - W_{\text{f}}$ per ion, where U_{iz} is the ionization energy [9, 31].

3.2. Choice of initial conditions

Dust dynamics simulations require initial conditions on the dust position, velocity, size and temperature as input. Although the injection experiment was designed to minimize the uncertainty in these initial conditions, the diversity of the observed trajectories shown in figure 2 reveals a non-negligible spread in position and velocity, likely due to slight velocity deviations caused by collisions with the 180 cm long injector tube or between the particles themselves during their supposed free fall. Such a spread in initial conditions results in dust particles sampling different paths through the inhomogeneous plasma, and hence in a variety of outcomes: particles that cross the hot and dense central regions are expected to reach higher temperatures and undergo stronger vaporization than those that remain in the peripheral plasma. A small fraction of the particles in figure 2 can even be seen to acquire a net upward velocity, which can be reproduced in MIGRAINE simulations through the azimuthal ion drag force caused by the rotation of the plasma column (see figure 6).

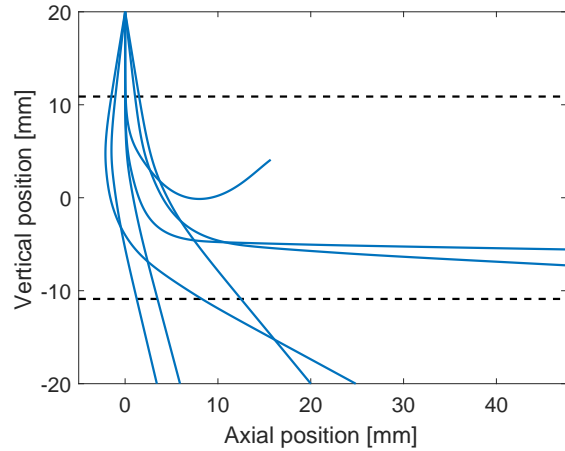


Figure 6. Examples of MIGRAINE trajectories resulting from the initial condition scan. Dashed lines indicate where the plasma density drops to 10 % of its central value. Note that the simulations assume translational symmetry along the plasma axis, hence all simulated particles are injected at the same axial position, here defined as zero. Any meaningful comparison with figure 2 must consider only differences of axial position within a given trajectory.

Considering the variability observed in camera images, dust detected by a given optical fiber may have very different temperature and size, depending on its past trajectory. In an attempt to reproduce this variability, the initial positions and velocities selected for MIGRAINE simulations were spread around nominal values: particles were injected from a horizontal disk of 6 mm diameter centered 2 cm directly above the plasma column, and their nominal downward velocity of 5 m s^{-1} was shifted by a random component up to 1 m s^{-1} in any direction. The initial radius was varied uniformly between 4 and $5 \mu\text{m}$ to mimic the narrow size distribution of the injected population, and the initial temperature remained fixed at 300 K. The resulting MIGRAINE trajectories shown in figure 6 reproduce the experimental data qualitatively in terms of overall trajectory shape and dust velocity evolution. Note that, due to the translational symmetry of the plasma profiles, simulated trajectories are independent of the initial axial particle position, hence all simulated particles are launched from the same axial position. Nevertheless, the statistical weight of each set of initial conditions cannot be reliably estimated from the measurements. This is mainly due to the absence of measurements of the dust position along the camera line of sight, on which the simulated trajectories were found to depend rather strongly. By default, all the simulated trajectories were assumed to be equally probable, and spectroscopic measurements were emulated by recording the vertical position, size and temperature of each dust particle at every simulation time step, with the exception of particles

colder than 2000 K, assumed to be undetectable in the experiment.

4. Results and comparison with simulations

4.1. Temperature and radius distributions

By virtue of the spatial resolution of the spectroscopic measurement system, it is possible to account for how the measured dust temperatures and radii depend on the vertical position of the particles. The distributions of measured dust temperature and radius are presented in figures 7 and 8 for the main shots of interest, after the removal of unphysical data points with $T_d > 7000$ K or $R_d > 10 \mu\text{m}$ (the number of excluded particles is given in table 1). A clear dependence on the particles' vertical position could be observed for the dust temperature, whereas the effect on the dust radius was much milder and limited to the statistical spread of the measurements.

All four shots share similar trends, with a peaked T_d profile and more data points near the center of the plasma column. The measured radii are consistently smaller than those of the injected dust, suggesting that vaporization takes place even during shots #189–191, where no anomalous emission signals were detected. In order to conduct a meaningful comparison with numerical simulations, the following discussions will be mostly focused on shot #189, which produced the most statistically reliable data.

4.2. Evidence of the work function contribution to electron heat fluxes

The impact of the work function contribution on MIGRAINE dust temperature and radius distributions for shot #189 are presented in figure 9. Despite the numerous uncertainties discussed previously, it is clear that accounting for electron work function heating is necessary to reproduce the quantitative trends in the experimental data. Without it, the simulated dust particles cannot be heated above 5000 K even in the central plasma, which results in negligible vaporization mass loss and no alteration of the injected size distribution. Although this comparison focuses on shot #189, which produced the most reliable data, the same conclusions can be drawn from the measurements of shots #190–191.

4.3. Vapour shielding

The observation of W line emission signals in shots #194–197 raises the question of whether vapour shielding plays a role in the experiment. Within the uncertainties of our measurements, this does not appear to be the case, since no significant difference

can be observed in the distributions of T_d and R_d between shot #197 and those in which no anomalous emission was detected. Theoretical investigations of the potential importance of vapour shielding in dust heating [32] suggest that a critical dust radius exists, above which the shielding process cannot be neglected. In the context of our experiment, this critical radius is estimated between $1 \mu\text{m}$ and $10 \mu\text{m}$, preventing firm conclusions to be drawn.

5. Discussion and interpretation

5.1. Characteristic OML scalings

The purpose of this section is to explain why OML estimations reproduce the experimental data with reasonable accuracy and to explore the sensitivity of the results to various parameters. To this end, we will employ approximated formulae which capture the essential OML scalings for W dust in uniform plasmas with relevant densities and temperatures. Detailed justifications are provided in appendix and rely heavily on the fact that the evolution of a single dust grain can be split into three main stages:

(I) Initially, the dust is cold and non-emitting, hence its floating potential ϕ_d corresponds to equal electron and ion fluxes, namely $\phi_d \simeq -2.5 T_e/e$, where T_e is the background electron temperature and e is the elementary charge. The total heat flux received by the dust is approximately constant and T_d increases steadily.

(II) When T_d becomes large enough, thermionic emission starts and triggers a well-known instability [2] whereupon the shift of ϕ_d towards positive values enhances the total incoming heat flux, leading to stronger thermionic emission and a further increase of ϕ_d . As a result, the dust becomes positively charged, implying that collection fluxes become comparable to their thermal values and that ions can be neglected due to their large mass: the floating condition equates the background and thermionic electron fluxes, corresponding to a value of ϕ_d of the order of T_d/e . For a hot enough plasma, $T_d \ll T_e$ implies that $e\phi_d/T_e \ll 1$. The dust temperature increases at a higher rate than in stage (I) and vaporization starts.

(III) The dust particle enters the strong vaporization regime — which is characterized by the fact that all the incoming energy is spent into ablating dust material — and T_d settles into a steady state. The dust radius decreases at a constant rate until complete vaporization is reached.

Neglecting the duration of the transitional stage (II), which is typically very short on account of its instability-driven nature, dust particles in the central regions of the Pilot-PSI plasma can be assumed to be in the strong vaporization stage (III). In this

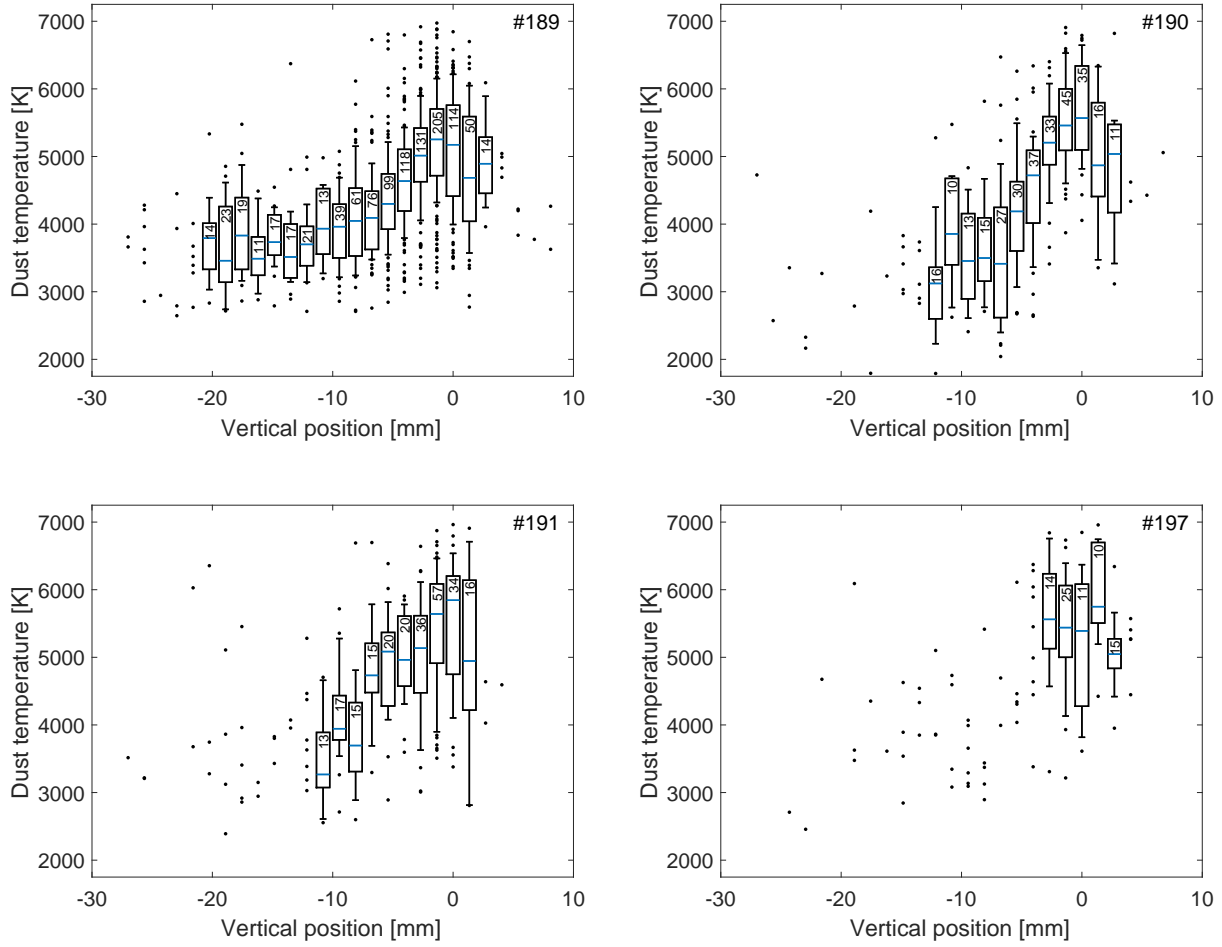


Figure 7. Box plots illustrating the spatial dependence of the measured dust temperature for the four shots of interest. Boxes are shown only for samples consisting of at least 10 measurements, in which case the sample size is indicated in the box. The whiskers extend over the interdecile range.

stage, the steady-state dust temperature T_d^{vap} can be approximated as

$$T_d^{\text{vap}} \simeq \frac{T_{\text{scale}}}{\ln(q_{\text{scale}}/q_0)}, \quad (2)$$

where the scaling constants T_{scale} and q_{scale} depend only on the thermodynamic properties of W, and q_0 is the thermal electron plasma heat flux,

$$q_0 = n_e T_e \sqrt{\frac{2T_e}{\pi m_e}}, \quad (3)$$

in which n_e is the background electron density and m_e is the electron mass. Similarly, the dust lifetime t_{life} can be estimated by adding the characteristic duration of the heating stage (I) and the time required to reduce the dust radius from its initial value R_d^0 to zero during stage (III). This results in

$$t_{\text{life}} \simeq C \frac{R_d^0}{q_0}, \quad (4)$$

where the constant C is determined mostly by the thermodynamic properties of the dust material.

5.2. Sensitivity of the dust temperature and radius to plasma parameters

A remarkable feature of the experimental results presented in section 4.1 is the fact that, despite sizeable differences in plasma density and temperature between shots #189–191 and #194, no significant variations can be observed in the measured distributions of T_d . In fact, this trend can be reproduced by MIGRAINE simulations implementing the most ‘extreme’ plasma profiles relevant to the experiment, namely the hot dense plasma of shot #196 and cold sparse plasma of shot #209. The resulting dust temperature

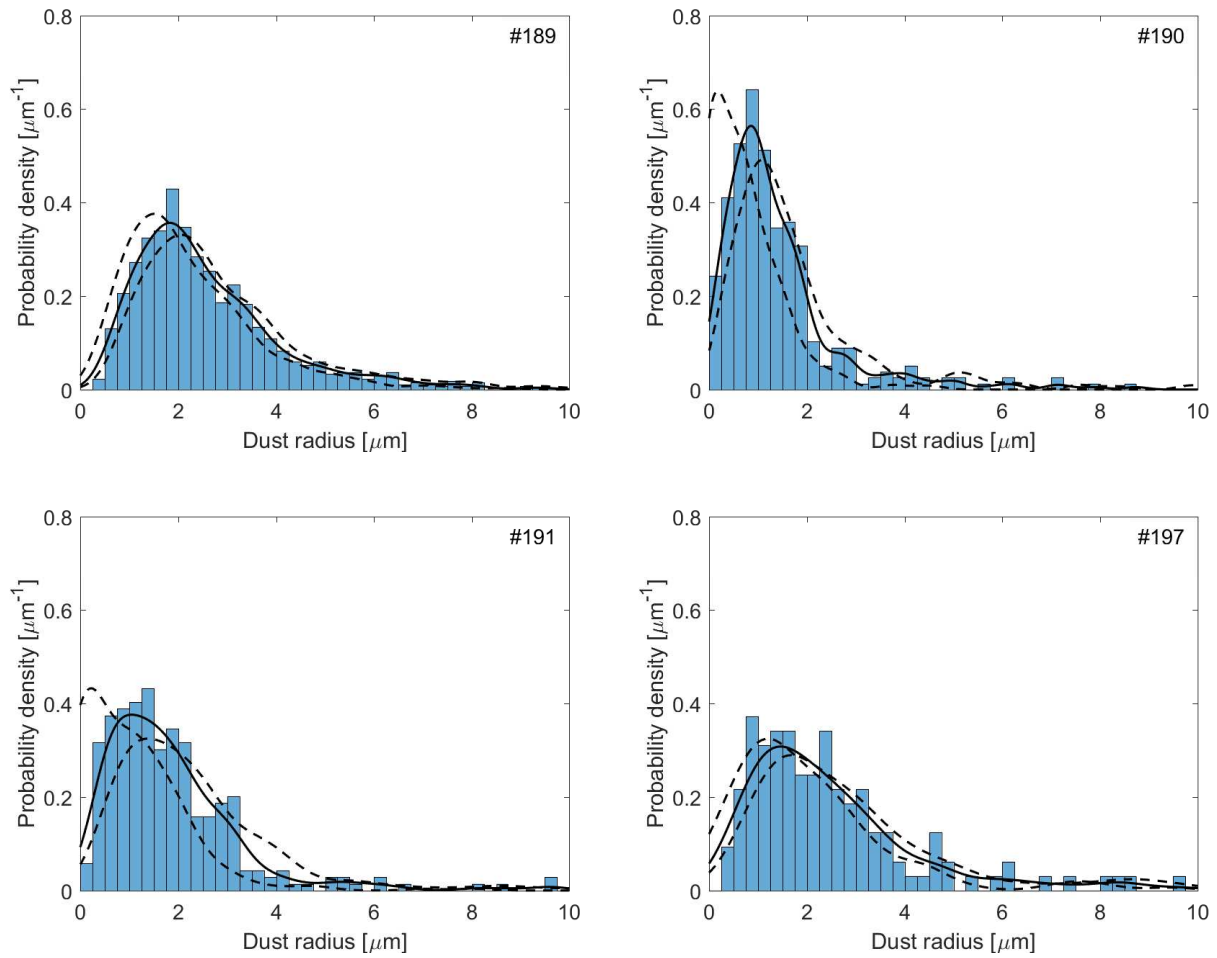


Figure 8. Histograms of the measured dust radius for the four shots of interest, together with gaussian kernel density estimates (solid curves). The dashed curves represent the gaussian kernel density estimates obtained by shifting the measured radii along their error bar.

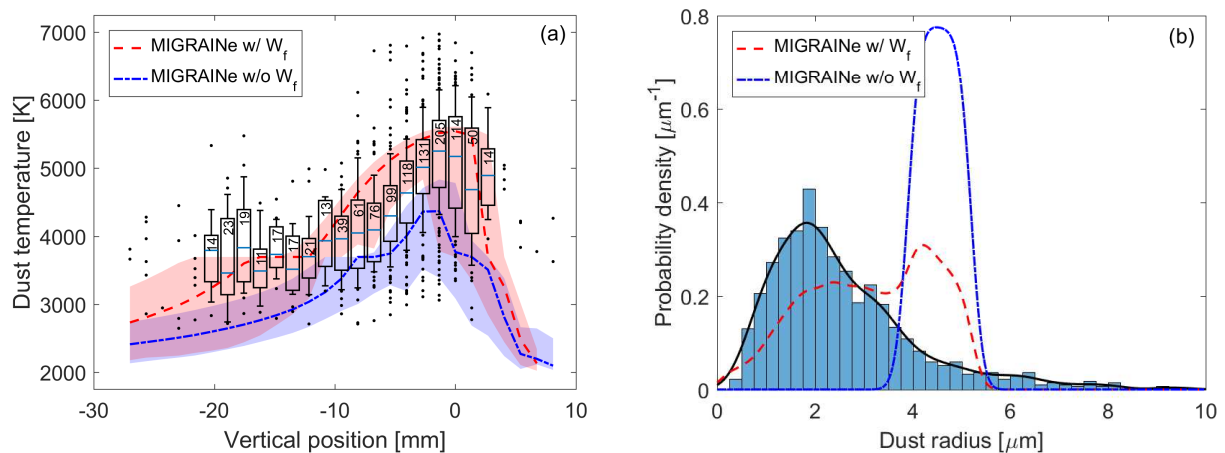


Figure 9. Comparison between spectroscopic measurements of dust temperature (a) and radius (b) for shot #189 and MIGRAINE simulations run with and without the electron work function heating term. The data is presented as in figures 7 and 8. MIGRAINE dust temperature distributions in (a) are represented by their median (curves) and interdecile range (shaded area).

distributions are plotted in figure 10(a) and their difference is shown to be negligible with respect to the experimental accuracy. From the theoretical standpoint, the low sensitivity of the dust temperature can be understood from (2), which predicts that a tenfold increase of q_0 from 50 to 500 MW m⁻² — which covers the relevant range of plasma environments in our experiments — results in an increase of T_d^{vap} by 15 % only. A similar phenomenon was pointed out in [33] regarding vapour shielding simulations for plasma-facing components, in which the maximum thermal energy that can be accumulated in a material target was found to depend very weakly on the physical model employed to describe vapour shielding.

A more pronounced difference can be observed on the distributions of simulated radii shown in figure 10(b), reflecting the fact that dust vaporization is stronger in shot #196. This is consistent with our interpretation that the anomalous spectral signal measured during shots #194–197 are caused by line emission from vaporized W.

5.3. Role of thermionic emission

Given the critical role played by thermionic emission on the evolution of W dust, it would be natural to postulate that uncertainties in thermionic emission modelling have a deep impact on the predicted dust dynamics. In the MIGRAINE simulations presented in this paper, the thermionic emission current I_{TE} from negatively charged dust was calculated according to the Richardson-Dushman formula

$$I_{\text{TE}} = 4\pi R_d^2 A T_d^2 \exp\left(-\frac{W_f}{T_d}\right), \quad (5)$$

where the value of the so-called Richardson constant was set at $A = 60 \text{ A cm}^{-2} \text{ K}^{-2}$, which is the recommended value for solid W [34]. In case of positive dust potential $\phi_d \geq 0$, the current was corrected by a factor $(1 + e\phi_d/T_d) \exp(-e\phi_d/T_d)$ to account for the return current due to electrons that cannot escape the attractive dust potential. In fact, several sources of uncertainty exist that can degrade the accuracy of (5):

(i) The Schottky effect [35], which consists in an apparent reduction of the work function caused by the electric field at the surface of negatively charged dust. Quantitative corrections for this effect were included in the original version of MIGRAINE [6], but have been omitted due to the inaccuracy of the formulae commonly used to estimate the dust electric charge [36].

(ii) The formation of a potential well around strongly emitting dust, which has been shown to reduce the thermionic currents by up to 50 % and enhance dust survivability [18, 30].

(iii) The presence of the magnetic field, which can cause the emitted electrons to be promptly re-collected by the dust particle within their first gyro-orbit, thereby reducing the net emission current. Ignoring the sheath electric field, this effect can be quantified by integrating known results for planar surfaces with oblique magnetic field [37] over the spherical geometry of the dust surface, leading to a representative reduction of 60 % in the zero Larmor radius limit. More detailed calculations assuming a monotonic sheath potential yield comparable results [19]. Fully self-consistent estimations, e.g. by particle-in-cell simulations for planar surfaces [38, 39], have not been achieved yet and pose a major challenge in postulating appropriate boundary conditions in the pre-sheath.

(iv) Differences in electronic structure between solid and liquid metals are likely to alter the Richardson constant A , making it closer to its ideal, free-electron-model value $A_0 = 120 \text{ A cm}^{-2} \text{ K}^{-2}$.

Overall, the current calculated from (5) is expected to be accurate within a factor 2. In order to estimate the impact of this uncertainty on OML predictions, full MIGRAINE simulations of W dust heating in a uniform plasma — including second-order processes not discussed here, such as ion backscattering and thermal radiation cooling [6] — have been run with a corrective factor in (5), such that I_{TE} ranged between half and twice its nominal value. The resulting steady-state vaporization temperature and dust lifetime are shown in figure 11, which reveals that variations in thermionic emissions actually have a very weak effect. As before, the results appear to depend mainly on q_0 and are in remarkable agreement with the simplified scalings (2) and (4). The only appreciable deviations occur for $q_0 < 100 \text{ MW m}^{-2}$. In such cold plasmas, the assumption $e\phi_d/T_e \ll 1$ for positive dust does not hold during stage (III) and stronger thermionic emission leads to a significant shift of ϕ_d toward positive values, hence an increase of the electron collection heat flux and a reduced dust lifetime.

6. Conclusions

The first direct measurements of tungsten dust temperature and radius in cold and dense plasmas mirroring the conditions expected in the divertor of ITER have been carried out in Pilot-PSI, based on the analysis of thermal radiation spectra emitted by the dust particles. In spite of a controlled particle injection procedure and the preparation of a mono-disperse dust size population, the detailed validation of dust heating models was impeded by several issues connected to the experimental design as well as the specifics of the plasma regime addressed.

The difficult exploitation of the experimental

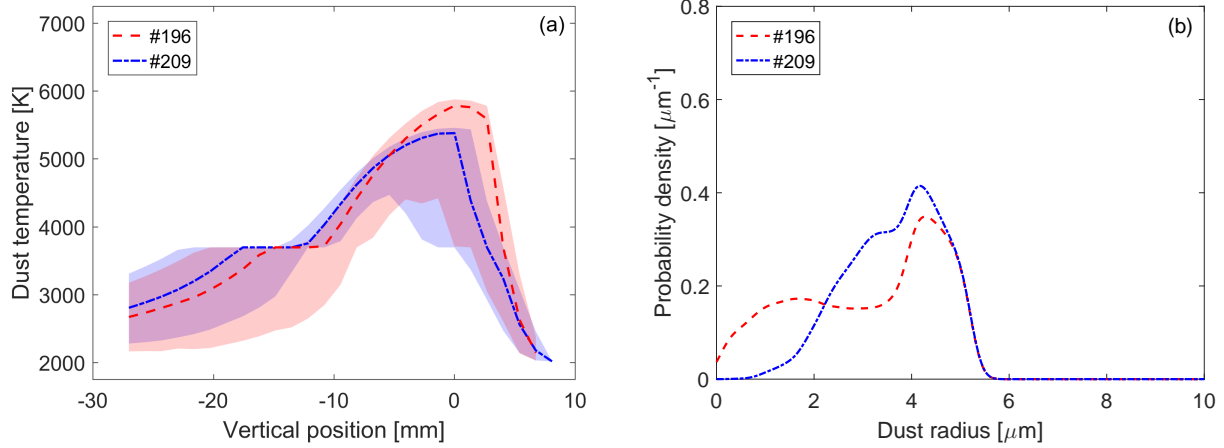


Figure 10. MIGRAINE distributions of dust temperature (a) and radius (b) for shots #196 and #209, including the electron work function heating term. Temperature distributions in (a) are represented by their median (curves) and interdecile range (shaded area).

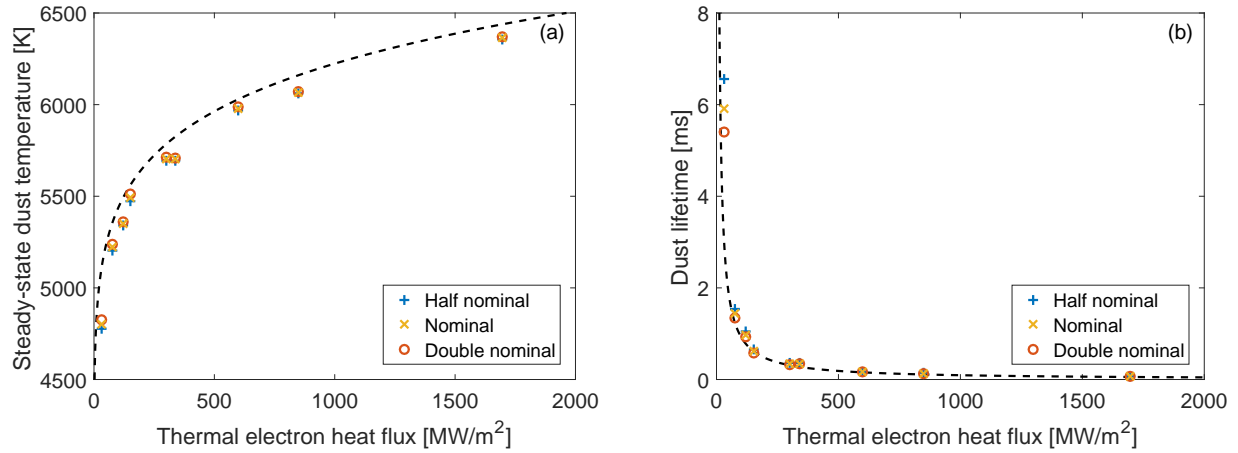


Figure 11. MIGRAINE simulations of a W grain with initial radius $1 \mu\text{m}$ and temperature 300 K in a uniform plasma whose electron density $n_e = 2\text{--}10 \times 10^{20} \text{ m}^{-3}$ and temperature $T_e = 2\text{--}10 \text{ eV}$ were scanned independently. The intensity of thermionic emission was varied between half and twice its nominal value (5). The steady-state dust temperature (a) and dust lifetime (b) are plotted as a function of the thermal electron heat flux as defined by (3). Approximated OML scalings (2) and (4) are plotted as black dashed curves.

results is only partially due to technical design issues, such as the narrow spectral observation window which affects the accuracy of the dust temperature and radius estimates. Other factors, in particular the high sensitivity of the dust particles' trajectory and heating history to slight variations in initial conditions, which is connected to the steep density and temperature gradients in Pilot-PSI, are unavoidable unless one can achieve the ideal situation of a large homogeneous fusion-relevant plasma in the laboratory. These considerations impose a statistical perspective on the dust temperature evaluations: only spatial distributions of the dust temperature, accounting for

the multitude of possible dust trajectories, could be analyzed meaningfully.

However, more profound theoretical obstructions to dust code validation reside in the fact that tungsten dust heating in the plasmas studied here belongs to the so-called strong vaporization regime. In this regime, OML-based models predict that the dust temperature depends mainly on the plasma parameters, such that various known inaccuracies in the detailed modelling of dust-plasma interactions become masked. This implies that attempts at using refined physical models targeting, for example, the inhibition of ion collection due to thin-sheath

effects [17], and the modification of electron emission currents by space charge effects [18] or the presence of a magnetic field [19], have no practical consequences on the predicted dust temperature and life time as far as one is bound by the OML framework. Moreover, the insensitivity of the dust temperature to the plasma parameters in this regime makes it a poor figure of merit for heating model validation, unless the experimental conditions allow very wide ranges of plasma heat flux to be explored. This can be compared to the similar conclusions of [33] on vapour shielding model validations based on matching the value of the saturation threshold of the energy deposited in a vaporizing plasma-exposed target.

On the other hand, the remarkable robustness of OML predictions gives rise to simple numerical scalings which were validated against full MIGRAINE simulations and shown to be sufficient to understand the main physics at play in such cold and dense plasmas. Furthermore, the comparison between the experimental results and MIGRAINE simulations in several plasma scenarios allowed firm conclusions to be drawn on some aspects of the heat balance of tungsten dust in cold and dense plasmas. In particular, the dominating contribution of the micro-physical processes occurring near the dust surface to dust heating, namely the release of binding energies upon plasma species collection, has clearly emerged from both experimental and simulation data. While this last conclusion holds for real ITER divertor plasmas, other conclusions drawn from OML-based analyses cannot be extrapolated. In fact, the effects of strong magnetic fields on background electron collection changes the core physics of dust charging and heating [8].

Acknowledgments

This work has been carried out within the framework of the EUROfusion Consortium (WPPFC) and has received funding from the Euratom research and training programme 2014–2018 under grant agreement No 633053. The views and opinions expressed herein do not necessarily reflect those of the European Commission. SR and PT would also like to acknowledge the financial support of the Swedish Research Council.

Appendix A. Derivation of approximated OML scalings for uniform plasmas

The purpose of this appendix is to delve into the details of the simplified OML scalings employed in section 5.1. We consider a single W dust particle, initially at room temperature and immersed in a uniform isothermal stationary hydrogen plasma. We

assume that dust charging is driven by three processes: electron collection, ion collection and thermionic emission. In addition to those, ion backscattering and ion surface neutralization contribute to dust heating, with the assumption that all impinging ions recombine on the dust surface regardless of whether they are subsequently backscattered.

During stage (I), no thermionic emission is considered and dust charging obeys the standard floating condition $\Gamma_e = \Gamma_i$, where the electron and ion fluxes are given by the standard OML formulas

$$\Gamma_e = \Gamma_0 \exp \varphi_d , \quad (\text{A.1})$$

$$\Gamma_i = \Gamma_0 \sqrt{\frac{m_e}{m_i}} (1 - \varphi_d) , \quad (\text{A.2})$$

with $\Gamma_0 = q_0/2T_e$ the thermal electron flux, m_i the ion mass and $\varphi_d = e\phi_d/T_e$ the normalized dust potential. Neglecting ion surface binding owing to the large ion backscattering yields of hydrogen on W [40], the total net heat flux received by the dust can then be written as

$$q_I = q_e^{\text{kin}} + (1 - R_i) q_i^{\text{kin}} + \Gamma_e W_f + \Gamma_i (U_{iz} - W_f) , \quad (\text{A.3})$$

where the kinetic contributions are also given by OML formulas

$$q_e^{\text{kin}} = q_0 \exp \varphi_d , \quad (\text{A.4})$$

$$q_i^{\text{kin}} = q_0 \sqrt{\frac{m_e}{m_i}} \left(1 - \varphi_d + \frac{\varphi_d^2}{2} \right) , \quad (\text{A.5})$$

R_i denotes the effective backscattered ion energy fraction, and the last two terms correspond to the equilibration of collected electrons and ion surface neutralization, respectively. Taking $R_i = 0.7$ for low-energy hydrogen ions on W [40] and solving for the floating potential, the total net heat flux can be written approximately as

$$q_I \simeq \left(0.13 + 0.04 \frac{U_{iz}}{T_e} \right) q_0 \simeq 0.27 q_0 , \quad (\text{A.6})$$

in which the second approximation has been obtained by taking the average value of $(13.6 \text{ eV})/T_e$ for T_e between 1 eV and 10 eV.

During stage (III), assuming that $T_d \ll T_e$ and $e\phi_d/T_e \ll 1$, the role of ions can be neglected and the floating condition reads $\Gamma_0 = \Gamma_e = \Gamma_{\text{TE}}$. Following the same reasoning as before, the net heat flux due to electron collection and emission can be written

$$q_{\text{III}} = q_e^{\text{kin}} - q_{\text{TE}}^{\text{kin}} + \Gamma_e W_f - \Gamma_{\text{TE}} W_f \simeq q_0 . \quad (\text{A.7})$$

The strong vaporization regime, which defines stage (III), is characterized by $q_{\text{III}} = q_{\text{vap}}$, where q_{vap} is the cooling flux due to surface vaporization. It can be expressed via the Hertz-Knudsen formula [41],

$$q_{\text{vap}}(T_{\text{d}}) = \Delta h_{\text{vap}} \sqrt{\frac{m_{\text{d}}}{2\pi T_{\text{d}}}} P_{\text{vap}}(T_{\text{d}}), \quad (\text{A.8})$$

where Δh_{vap} is the specific enthalpy of vaporization, m_{d} the mass of one dust atom and P_{vap} the vapour pressure of the dust material. Using a standard Antoine equation fit for the vapour shielding of W, $P_{\text{vap}} \propto \exp(-T_{\text{scale}}/T_{\text{d}})$, and retaining only the dominant exponential dependence on T_{d} by setting $T_{\text{d}} = 6000$ K (i.e. near the boiling point of W) under the square root in (A.8), leads to

$$q_{\text{vap}}(T_{\text{d}}) \simeq q_{\text{scale}} \exp\left(-\frac{T_{\text{scale}}}{T_{\text{d}}}\right), \quad (\text{A.9})$$

with $q_{\text{scale}} = 7.7 \times 10^{14}$ W m⁻² and $T_{\text{scale}} = 9.87 \times 10^4$ K [42]. Hence the estimation of the steady-state vaporization temperature $T_{\text{d}}^{\text{vap}}$ (2).

The duration of stages (I) and (III) are obtained from the dust heating equation, which governs the evolution of the dust specific enthalpy h_{d} . During stage (I), the dust radius remains constant at R_{d}^0 and the heating equation reads

$$\frac{1}{3} \rho R_{\text{d}}^0 \frac{dh_{\text{d}}}{dt} = q_{\text{I}}, \quad (\text{A.10})$$

where ρ is the mass density of the dust material. Using (A.6), the duration t_{I} of stage (I) can be written

$$t_{\text{I}} \simeq 1.23 \frac{\rho R_{\text{d}}^0 \Delta h_{\text{I}}}{q_0}, \quad (\text{A.11})$$

where Δh_{I} is the characteristic gain of specific enthalpy corresponding to a rise of T_{d} from room temperature to $T_{\text{d}}^{\text{vap}}$. During stage (III), h_{d} is constant and the heating equation actually describes the decrease of R_{d} due to vaporization fluxes:

$$\rho \frac{dR_{\text{d}}}{dt} = -\frac{q_{\text{vap}}}{\Delta h_{\text{vap}}} = -\frac{q_0}{\Delta h_{\text{vap}}}. \quad (\text{A.12})$$

Therefore, the duration of stage (III) corresponds to the time required to reduce R_{d} from R_{d}^0 to 0:

$$t_{\text{III}} = \frac{\rho R_{\text{d}}^0 \Delta h_{\text{vap}}}{q_0}. \quad (\text{A.13})$$

Using the room-temperature value $\rho = 19250$ kg m⁻³ during stage (I), the near-boiling-point value $\rho = 14000$ kg m⁻³ during stage (III) [43], $\Delta h_{\text{vap}} = 4.39$ MJ kg⁻¹ and $\Delta h_{\text{I}} = 1.36$ MJ kg⁻¹, corresponding to a tungsten temperature rise from 300 K to 6000 K, one obtains the approximation (4) with $C = 9.36 \times 10^{10}$ J m⁻³.

References

- [1] Pigarov A Y, Krasheninnikov S I, Soboleva T K and Rognlien T D 2005 *Phys. Plasmas* **12** 122508
- [2] Smirnov R D, Pigarov A Y, Rosenberg M *et al.* 2007 *Plasma Phys. Control. Fusion* **49** 347
- [3] Martin J D, Bacharis M, Coppins M *et al.* 2008 *Europhys. Lett.* **83** 65001
- [4] Delzanno G L and Tang X 2014 *Phys. Plasmas* **21** 022502
- [5] Autricque A, Hong S H, Fedorczak N *et al.* 2017 *Nucl. Mater. Energy* **12** 599
- [6] Vignitchouk L, Tolias P and Ratynskaia S 2014 *Plasma Phys. Control. Fusion* **56** 095005
- [7] Mott-Smith H M and Langmuir I 1926 *Phys. Rev.* **28** 727
- [8] Vignitchouk L, Ratynskaia S and Tolias P 2017 *Plasma Phys. Control. Fusion* **59** 104002
- [9] Vignitchouk L, Ratynskaia S, Tolias P *et al.* 2018 *Nucl. Fusion* **58** 076008
- [10] Roquemore A L, Nishino N, Skinner C H *et al.* 2007 *J. Nucl. Mater.* **363** 222
- [11] Rudakov D L, Litnovsky A, West W P *et al.* 2009 *Nucl. Fusion* **49** 085002
- [12] Shalpegin A, Vignitchouk L, Erofeev I *et al.* 2015 *Plasma Phys. Control. Fusion* **57** 125017
- [13] Brochard F, Shalpegin A, Bardin S *et al.* 2017 *Nucl. Fusion* **57** 036002
- [14] De Temmerman G, Bacharis M, Dowling J *et al.* 2010 *Nucl. Fusion* **50** 105012
- [15] Smirnov R D, Krasheninnikov S I, Pigarov A Y *et al.* 2011 *J. Nucl. Mater.* **415** S1067
- [16] Willis C T N, Coppins M, Bacharis M and Allen J E 2012 *Phys. Rev. E* **85** 036403
- [17] Bacharis M 2014 *Phys. Plasmas* **21** 074501
- [18] Delzanno G L and Tang X Z 2014 *Phys. Rev. Lett.* **113** 035002
- [19] Autricque A, Fedorczak N, Khrapak S A *et al.* 2017 *Phys. Plasmas* **24** 124502
- [20] Marenkov E D and Krasheninnikov S I 2014 *Phys. Plasmas* **21** 123701
- [21] Krasheninnikov S I and Marenkov E D 2015 *J. Nucl. Mater.* **463** 869
- [22] Kantor M, Tsalas M, Litnovsky A *et al.* 2013 *J. Nucl. Mater.* **438** S711
- [23] Westerhout J, Koppers W R, Vijvers W A J *et al.* 2007 *Phys. Scr.* **T128** 18
- [24] de Groot B, Al R S, Engeln R *et al.* 2007 *Fusion Eng. Des.* **82** 1861
- [25] Endstrasser N, Brochard F, Rohde V *et al.* 2011 *J. Nucl. Mater.* **415** S1085
- [26] Bohren C F and Huffman D R 1983 *Absorption and Scattering of Light by Small Particles* (New York: Wiley Interscience)
- [27] Roberts S 1959 *Phys. Rev.* **114** 104
- [28] Demidov V I, Ratynskaia S V and Rypdal K 2002 *Rev. Sci. Instrum.* **73** 3409
- [29] Tolias P 2016 Low energy electron reflection from tungsten surfaces (*Preprint arXiv:1601.02047v1*)
- [30] Vignitchouk L, Delzanno G L, Tolias P and Ratynskaia S 2018 *Phys. Plasmas* **25** 063702
- [31] Komm M, Ratynskaia S, Tolias P *et al.* 2017 *Plasma Phys. Control. Fusion* **59** 094002
- [32] Brown B T, Smirnov R D and Krasheninnikov S I 2014 *Phys. Plasmas* **21** 024501
- [33] Skovorodin D I, Pshenov A A, Arakcheev A S *et al.* 2016 *Phys. Plasmas* **23** 022501
- [34] Fomenko V 1966 *Handbook of Thermionic Properties: Electronic Work Functions & Richardson Constants of Elements and Compounds* (New York: Plenum Press)
- [35] Herring C and Nichols M H 1949 *Rev. Mod. Phys.* **21** 185
- [36] Tang X Z and Delzanno G L 2014 *Phys. Plasmas* **21** 123708

- [37] Igitkhanov Y and Janeschitz G 2001 *J. Nucl. Mater.* **290** 99
- [38] Komm M, Tolias P, Ratynskaia S *et al.* 2017 *Phys. Scripta* **T170** 014069
- [39] Komm M, Ratynskaia S, Tolias P *et al.* 2017 *Plasma Phys. Control. Fusion* **59** 094002
- [40] Eckstein W 2009 Reflection (backscattering) Tech. Rep. IPP 17/12 Max Planck Institute for Plasma Physics
- [41] Dushman S and Lafferty J M 1962 *Scientific Foundations of Vacuum Technique* (New York: Wiley)
- [42] Plante E and Sessoms A 1973 *J. Res. Natl Bur. Stand.* **77A** 237
- [43] Tolias P 2017 *Nucl. Mater. Energy* **13** 42